

Transtensional Rupture within a Diffuse Plate Boundary Zone during the 2020 M_w 6.4 Puerto Rico Earthquake

Renier Viltres^{*†1}, Adriano Nobile^{†1}, Hannes Vasyura-Bathke^{1,2}, Daniele Tripanera¹, Wenbin Xu³, and Sigurjón Jónsson¹

Abstract

On 7 January 2020, an M_w 6.4 earthquake occurred in the northeastern Caribbean, a few kilometers offshore of the island of Puerto Rico. It was the mainshock of a complex seismic sequence, characterized by a large number of energetic earthquakes illuminating an east–west elongated area along the southwestern coast of Puerto Rico. Deformation fields constrained by Interferometric Synthetic Aperture Radar and Global Navigation Satellite System data indicate that the coseismic movements affected only the western part of the island. To assess the mainshock’s source fault parameters, we combined the geodetically derived coseismic deformation with teleseismic waveforms using Bayesian inference. The results indicate a roughly east–west oriented fault, dipping northward and accommodating ~1.4 m of transtensional motion. Besides, the determined location and orientation parameters suggest an offshore continuation of the recently mapped North Boquerón Bay–Punta Montalva fault in southwest Puerto Rico. This highlights the existence of unmapped faults with moderate-to-large earthquake potential within the Puerto Rico region.

Cite this article as: Viltres, R., A. Nobile, H. Vasyura-Bathke, D. Tripanera, W. Xu, and S. Jónsson (2021). Transtensional Rupture within a Diffuse Plate Boundary Zone during the 2020 M_w 6.4 Puerto Rico Earthquake, *Seismol. Res. Lett.* **XX**, 1–17, doi: [10.1785/0220210261](https://doi.org/10.1785/0220210261).

Supplemental Material

Introduction

On 28 December 2019, a seismic sequence started in the northeastern Caribbean, southwest of the Puerto Rico island, with an M_L 4.7 earthquake (Fig. 1; Liu *et al.*, 2020). At least 650 events with magnitude ≥ 3 , including 95 with magnitude ≥ 4 , occurred in the next 40 days (Fig. 2d; University of Puerto Rico, 1986). Most of the events nucleated at shallow depths (<20 km) over an east–west elongated area ($\sim 30 \times 50 \text{ km}^2$) ~ 30 km southwest of the city of Ponce, in front of Guayanilla bay (Fig. 2a,b,d). The earthquake locations align along three main directions, north-northeast to south-southwest, north-northwest to south-southeast, and east–west, whereas their focal mechanisms suggest two main families: 1) pure strike-slip and 2) normal faulting with a strike-slip component (Fig. 2a–c; University of Puerto Rico, 1986; United States Geological Survey [USGS], 2020).

The mainshock of the sequence struck on 7 January 2020, with a seismic moment release consistent with a M_w 6.4 earthquake (e.g., University of Puerto Rico, 1986). It was preceded by one day by a M_w 5.8 foreshock and followed by four $M_w \geq 5$ aftershocks in less than 12 hr. The ground shaking associated with these events produced significant damage to buildings and infrastructure in southwest Puerto Rico, and cost at least one casualty (López *et al.*, 2020; Miranda *et al.*, 2020). After 4 February, the daily number of earthquakes continued to

decrease with time, as the sequence shifted to sporadic bursts of seismicity accompanied by stronger events (University of Puerto Rico, 1986). The latest energetic aftershocks occurred on 3 July 2020, with a seismic moment release consistent with a M_w 5.3 earthquake and two with $M_L \geq 4.5$ on 24 December (University of Puerto Rico, 1986).

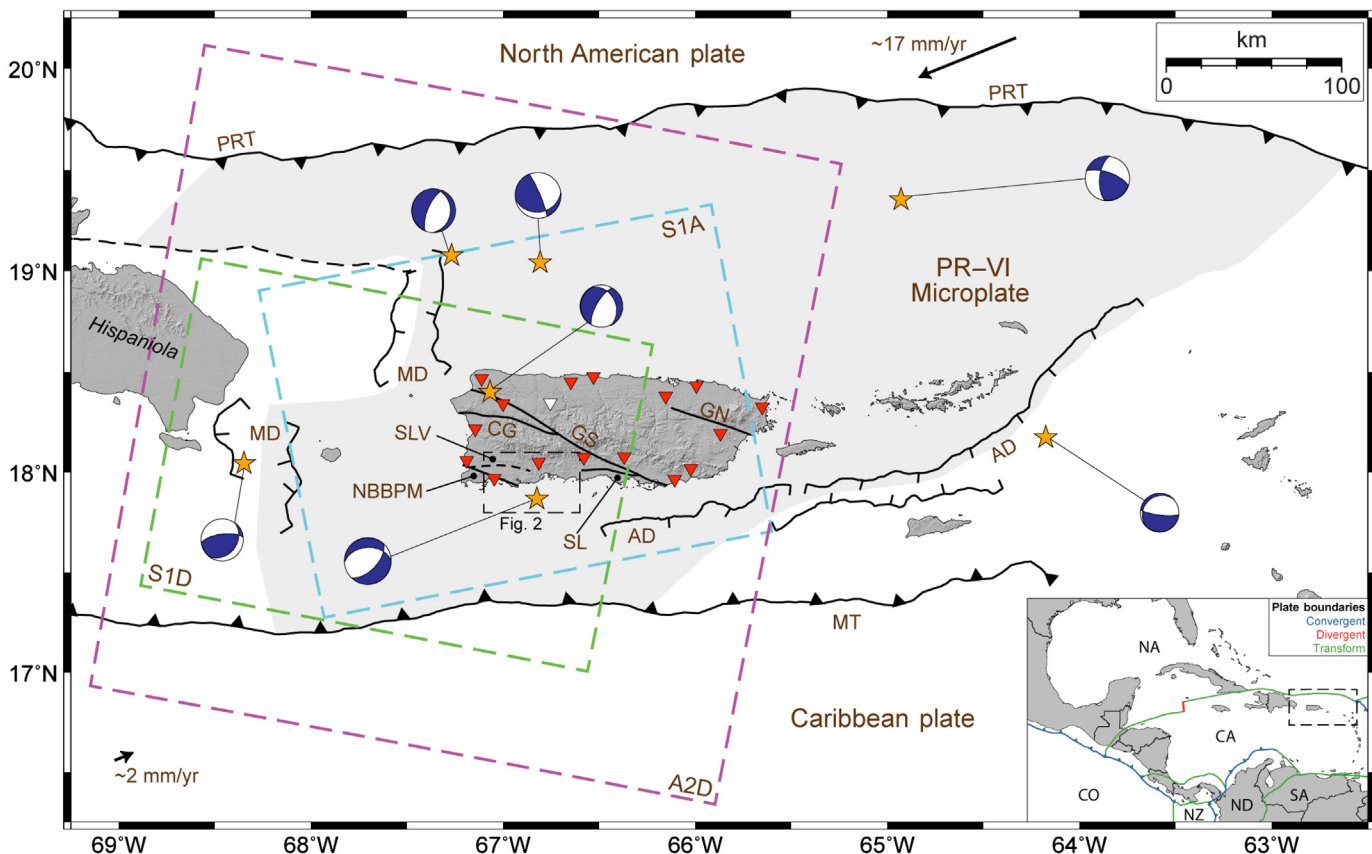
Since the early 1990s, Interferometric Synthetic Aperture Radar (InSAR) and Global Navigation Satellite System (GNSS) techniques have been widely used to study the earthquake-induced ground deformation, providing constraints on the location, orientation, extent, and slip associated with the rupturing faults (Massonnet *et al.*, 1993; Hudnut *et al.*, 1994; Jónsson *et al.*, 2002; Calais *et al.*, 2010; Dalla Via *et al.*, 2012; Fielding *et al.*, 2020). InSAR is more sensitive to vertical movements and inefficient in measuring displacements along the satellite’s flight direction (approximately north–south) (e.g., Hanssen, 2001),

1. Physical Science and Engineering Division, King Abdullah University of Science and Technology, Thuwal, Saudi Arabia, <https://orcid.org/0000-0002-4203-1417> (RV); <https://orcid.org/0000-0001-9528-7611> (AN); <https://orcid.org/0000-0002-3826-0663> (HV-B); <https://orcid.org/0000-0002-7028-3566> (DT); 2. Potsdam University, Potsdam, Germany; 3. School of Geosciences and Info-Physics, Central South University, Changsha, China, <https://orcid.org/0000-0001-7294-8229> (WX)

*Corresponding author: renier.ladrondeguevara@kaust.edu.sa

†These authors contributed equally to this work.

© Seismological Society of America



whereas GNSS provides better results for the horizontal components (Floyd *et al.*, 2010). Besides, the sparse 3D deformations with mm-level accuracy resolved by continuous GNSS observations enhance the cm-level accuracy line-of-sight (LOS) deformation imaging by InSAR. Thus, the two techniques are complementary, and their combination allows to produce cross-validated deformation measurements. Furthermore, GNSS ancillary data, like tropospheric signal delay estimations, can be used to reduce atmospheric signals in SAR interferograms (e.g., Li *et al.*, 2006; Cheng *et al.*, 2012). These datasets can be combined with seismological recordings to resolve for the spatiotemporal evolution of the rupture propagation (Delouis *et al.*, 2002; Salichon *et al.*, 2004; Delouis *et al.*, 2010; Konca *et al.*, 2010).

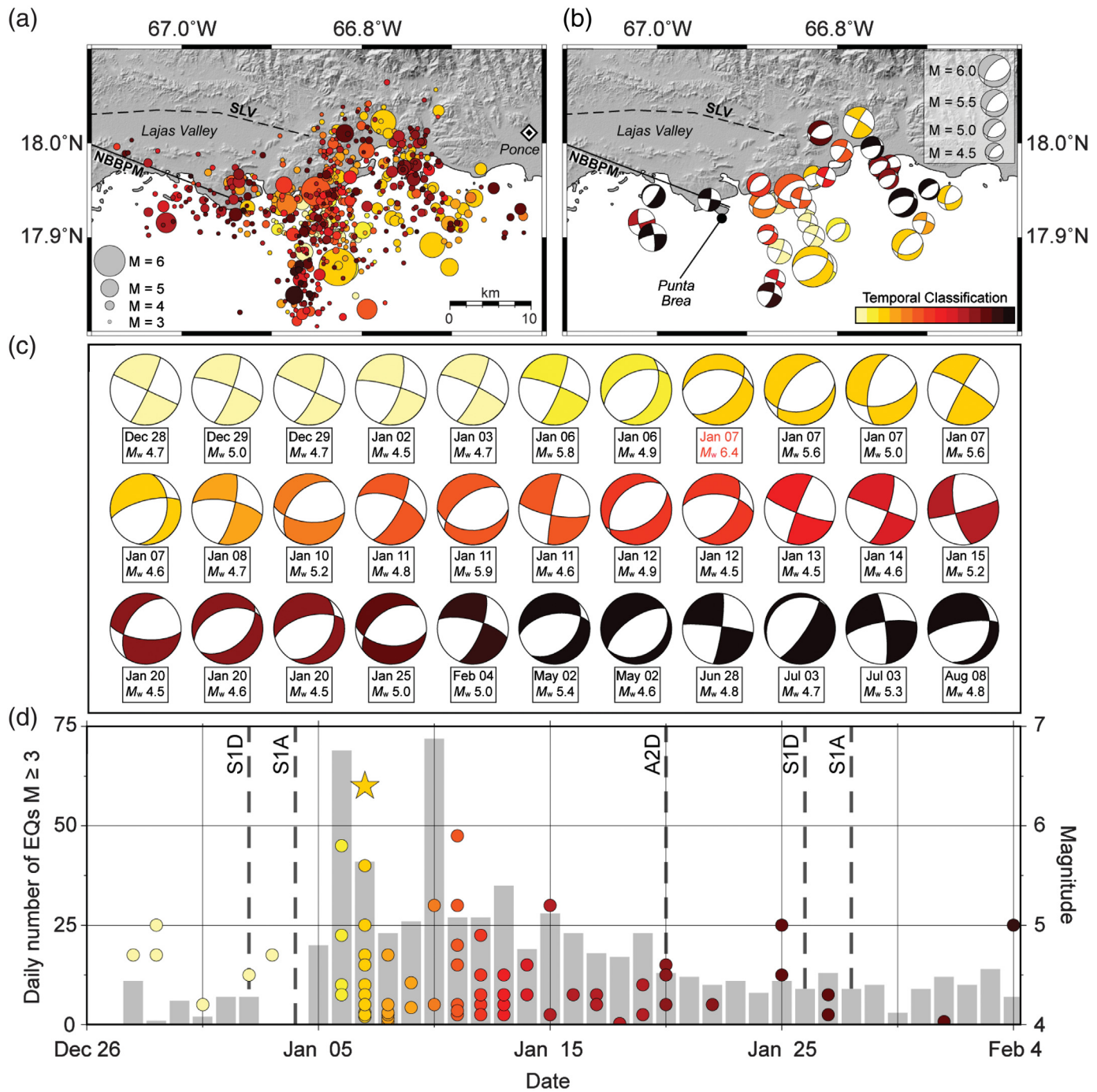
Here, we report on the onland coseismic deformation generated by the most energetic events of the 2019–2020 southwestern Puerto Rico seismic sequence using SAR images from the Sentinel-1 and the ALOS-2 satellites, and GNSS measurements from the Puerto Rico geodetic network. We then combine these independent deformation datasets with teleseismic waveform recordings to estimate the mainshock's source fault parameters using the Bayesian Earthquake Analysis Tool (BEAT; Vasyura-Bathke *et al.*, 2019, 2020). Finally, we compare our results with former geomorphological (e.g., Mann, Hippolyte, *et al.*, 2005; Prentice and Mann, 2005; Roig-Silva *et al.*, 2013; López *et al.*, 2020), kinematics (e.g., ten Brink and López-Venegas, 2012; Symithe *et al.*, 2015; Yang *et al.*, 2016; Wang *et al.*, 2019), and seismic (e.g., Huérano *et al.*, 2005;

Figure 1. Tectonic setting of the Puerto Rico (PR)–Virgin Island (VI) microplate (light gray) after Piety *et al.* (2018). Black arrows represent the plate motion relative to the PR–VI microplate defined after Jansma *et al.* (2000) and Huérano *et al.* (2005). Orange stars are $M_w > 4.5$ earthquake locations whose focal mechanisms indicate the general stress regime of the region. The cyan, green, and magenta boxes mark the footprints of the Sentinel-1 (S1A, S1D), and ALOS-2 (A2D) images, respectively. Inverted triangles are the Global Navigation Satellite System (GNSS) stations of the Puerto Rico geodetic network with station AOPR in white. The dashed-black box corresponds to the area in Figure 2a,b. Inset map shows the plate boundary configuration of the Caribbean region with color-coded boundary types. Black solid lines outline political boundaries. Abbreviations: Annegada Deep (AD), Caribbean plate (CA), Cerro Golden fault (CG), Coco plate (CO), Great Northern Puerto Rico fault (GN), Great Southern Puerto Rico fault (GS), Mona Deep (MD), Muertos trough (MT), Nazca plate (NZ), North American plate (NA), North Andes plate (ND), North Boquerón Bay–Punta Montalva fault (NBBPM), Puerto Rico Trench (PRT), Salinas fault (SL), South American plate (SA), and South Lajas Valley fault (SLV). The color version of this figure is available only in the electronic edition.

Clinton *et al.*, 2006; Liu *et al.*, 2020) studies in the area to constrain the tectonic framework associated with the rupture.

Tectonic Setting

The Puerto Rico Island lies on the Puerto Rico–Virgin Islands (PR–VI) microplate, located along the convergent boundary between the Caribbean and the North American plates



(Fig. 1). In particular, east-northeast oriented oblique double underthrusting takes place north and south of Puerto Rico at a convergence rate of ~ 2 cm/yr (Jansma *et al.*, 2000; Mann *et al.*, 2002; Jansma and Mattioli, 2005; Granja Bruña *et al.*, 2009). The oblique convergence direction along the plate boundary results in a complex geodynamic setting, characterized by oblique collision to the west, oblique subduction at the longitude of Puerto Rico, and frontal subduction to the east (Fig. 1; Calais *et al.*, 2016). As a consequence of this plate boundary setting, the transpressional strain regime in Hispaniola gradually becomes transtensional in the Puerto Rico area (Calais *et al.*, 2016).

Figure 2. Information about the 2019–2020 Puerto Rico earthquake sequence. (a) Spatial distribution of $\mathbf{M} > 3$ earthquakes that occurred between 28 December 2019 and 4 February 2020 color coded by date (after University of Puerto Rico, 1986). (b) Location and focal mechanisms for the largest 33 events of the earthquake sequence (University of Puerto Rico, 1986). (c) The focal mechanisms in panel (b) shown in a chronological order. (d) Number of $\mathbf{M} \geq 3$ earthquakes per day (gray bars) and $\mathbf{M} \geq 4$ events (circles) in the corresponding day. Vertical-dashed lines mark the Synthetic Aperture Radar (SAR) acquisition dates, and the orange star depicts the sequence's mainshock.

The PR-VI microplate is bounded to the north by the Puerto Rico Trench and to the south by the Muertos trough, resulting from the double underthrusting (Fig. 1). South of the Puerto Rico Trench, the deformation is mainly accommodated by three east–west oriented strike-slip fault zones, suggesting strike-slip instead of compressional strain regime north of Puerto Rico (Grindlay *et al.*, 2005; Mann, Hippolyte, *et al.*, 2005). These structures accommodate ~85% of the relative motion between the North American and the Caribbean plates, whereas the remnant motion is accommodated by the southern Muertos trough boundary and/or the onland fault systems in Puerto Rico (Fig. 1; Mann, Prentice, *et al.*, 2005; Prentice and Mann, 2005). Their dominant strike-slip strain regime, on the other hand, is consistent with the overall left-lateral strike-slip relative motion between the tectonic plates at the Puerto Rico longitude (DeMets *et al.*, 2000; Jansma *et al.*, 2000; Mann *et al.*, 2002; Jansma and Mattioli, 2005). The microplate is bounded to the west by the Mona Deep, where north–south oriented normal faults accommodate 1.5–3.9 mm/yr of east–west extension relative to the Hispaniola, since a few million years (Fig. 1; Jansma and Mattioli, 2005; Mann, Prentice, *et al.*, 2005; Calais *et al.*, 2016). To the southeast, the PR-VI microplate is bounded by the Anegada Deep (Huérzano *et al.*, 2005). The kinematics of this structure is still unclear; however, block models constrained by Global Positioning System measurements suggest a possible transtensional strain regime (Jansma and Mattioli, 2005; Symithe *et al.*, 2015; Calais *et al.*, 2016). The stronger earthquakes in this region ($4.5 \leq M_w \leq 6.4$) have mainly been located along the boundaries of the PR-VI microplate (University of Puerto Rico, 1986; Clinton *et al.*, 2006).

Despite the PR-VI microplate being usually considered a rigid block, several internal active faults are present within Puerto Rico (Grindlay *et al.*, 2005; Huérzano *et al.*, 2005; Mann, Prentice, *et al.*, 2005; Fig. 1). Inland, the Puerto Rico Island is affected by two major northwest–southeast oriented fault zones (hundreds of kilometers long) parallel to each other, the Great Northern (GN) and the Great Southern (GS) Puerto Rico, respectively (Piety *et al.*, 2018). The GS continues offshore both westward and eastward, where at least two Quaternary ruptures have been identified (Piety *et al.*, 2018; Fig. 1). Eastward, the GS strike curves to the northeast, as a consequence of the strain regime changing from strike-slip to mainly extensional (Mann, Hippolyte, *et al.*, 2005). Moreover, offshore faults with a similar orientation are considered seismically active (Jansma and Mattioli, 2005; and references therein).

Another potentially active fault is the east–west oriented Cerro Golden (CG; Laó-Dávila *et al.*, 2000; Mann, Prentice, *et al.*, 2005; Fig. 1). This fault is considered a splay structure of the GS affecting both the onshore and offshore part of western Puerto Rico (Jansma and Mattioli, 2005). Both normal and left-lateral strike-slip motions have been identified along the onshore and offshore parts of this fault zone during the Quaternary (Laó-Dávila *et al.*, 2000; Piety *et al.*, 2018).

According to Mann, Hippolyte, *et al.* (2005), the CG belongs to a large apical graben formed after the early Pliocene, as a consequence of crust arching in the western part of Puerto Rico.

An additional east–west oriented fault zone, affecting the southwest Puerto Rico, is the South Lajas Valley fault (SLV; Huérzano *et al.*, 2005; Mann, Prentice, *et al.*, 2005; Fig. 1). This structure continues westward offshore to the south of Mona Deep and shows a normal kinematics with a strike-slip component (Grindlay *et al.*, 2005; Prentice and Mann, 2005). Motion along the onshore faults of Puerto Rico is inferred to be ≤ 2 mm/yr, but the SLV has been considered a possible locus of the highest permissible onland deformation (Jansma and Mattioli, 2005). This is consistent with the fact that this is the area with the highest amount of microseismicity, although with only eight instrumental earthquakes with $4 \leq M_w \leq 4.6$ (University of Puerto Rico, 1986; Huérzano *et al.*, 2005; Clinton *et al.*, 2006).

The SLV is crosscut by the recently discovered west–northwest oriented North Boqueron Bay–Punta Montalva fault (NBBPM; Roig-Silva *et al.*, 2013; Adames-Corraliza, 2017). The fault zone shows strain partitioning between a dominant left-lateral strike-slip kinematics with east–west oriented displacements and smaller northwest oriented normal faults and extensional fractures. Although most of the deformation along the NBBPM is older than the Holocene, it is considered an active fault system (Roig-Silva *et al.*, 2013). Indeed, the 2019–2020 seismic sequence is located offshore along the southeastward continuation of this fault system (López *et al.*, 2020; Miranda *et al.*, 2020).

Adding to that, the offshore area south of Puerto Rico reveals the presence of northeast oriented normal faults accommodating southeast directed extension (Mann, Hippolyte, *et al.*, 2005). This observation is consistent with two successive phases of tectonic extension with north–northeast to south–southwest and northwest–southeast oriented motions, respectively, being identified in southwestern Puerto Rico (Mann, Hippolyte, *et al.*, 2005). The first phase took place during the Oligocene–Miocene and can be responsible for the formation of east–west trending tectonic features like the SLV (Mann, Hippolyte, *et al.*, 2005). Faults related to the second phase of extension crosscut preexisting tectonic structures and suggest a post-early Pliocene to Quaternary age of the deformation (Mann, Hippolyte, *et al.*, 2005). This last northwest–southeast oriented extension is expected to induce extensional motions on neighboring northeast trending faults and left-lateral strike-slip motions along northwest oriented faults such as the GS (Mann, Hippolyte, *et al.*, 2005).

Data and Methods

InSAR

The SAR images analyzed in this study come from the Sentinel-1A and ALOS-2 satellites, and were provided by

the European Space Agency and the Japan Aerospace Exploration Agency (ESA and JAXA), respectively (see [Data and Resources](#)). The Sentinel-1 satellites regularly acquire data over Puerto Rico every 12 days from both ascending (S1A) and descending (S1D) orbits in Interferometric Wide swath mode. We selected two pairs of images with 24-day time span (Fig. 2d), one for the ascending (4–28 January) and one for the descending (2–26 January) orbit, which provided interferograms with higher coherence and fewer artifacts than the 12 days observations. ALOS-2 acquires sporadically over the area, with only one ScanSAR Wide mode acquisition in descending orbit (A2D) available after the mainshock (20 January 2020) and the preseismic image acquired four months before (16 September 2019).

We processed all the interferograms with the GAMMA software ([Wegmüller, 1998](#)). To evaluate and remove the topographic phase component from the interferograms, the Shuttle Radar Topography Mission 1-arcsec digital elevation model ([Farr and Kobrick, 2000](#)) was used. The interferograms were multilooked to obtain $\sim 30 \text{ m} \times 30 \text{ m}$ pixels and filtered to increase the signal to noise ratio, and the coherence ([Goldstein and Werner, 1998](#)). The three selected interferograms were unwrapped using the minimum cost flow algorithm ([Werner et al., 2002](#)), manually corrected for obvious remnant unwrapping errors and converted into LOS displacement.

The Puerto Rico Island is located within a tropical environment characterized by highly variable water vapor content in the troposphere that results in strong atmospheric signals in the interferograms ([Hanssen, 2001](#)). To partially remove the atmospheric phase screen (APS), we used the GNSS-derived zenith delay estimations at each SAR acquisition time (e.g., [Li et al., 2006; Cheng et al., 2012](#)). The resulting maps are still affected by residual orbital ramps and topography correlated signals ([Hanssen, 2001](#)). We thus evaluated and removed a 3D surface that describes the interferometric phases as a linear combination of each pixel position (x, y, z) obtained by the least-squares method. The three final deformation maps refer to the same reference point that is considered stable and corresponds to the location of the AOPR GNSS station (Fig. 1). The remnant residual noise, here considered as the displacement error, was quantified by estimating the standard deviation in the area within 5 km of the stable reference point. This resulted in standard deviation of $\pm 2.3 \text{ cm}$ for the S1A, $\pm 2.7 \text{ cm}$ for S1D, and $\pm 3.8 \text{ cm}$ for A2D. Detailed information about all the corrections along with the cross validation with the GNSS data are described in the supplementary material (Texts S1 and S2; Figs. S1–S4).

Combining two or more different-looking geometries allows to obtain the near-east and vertical components of the ground displacement vector ([Dalla Via et al., 2012; Fuhrmann and Garthwaite, 2019](#)). Because the A2D and S1D images have similar-looking geometries, they provide redundant information for this estimation. However, A2D has a larger coverage

and higher coherence, and thus is more reliable in resolving cm-level displacements in relatively small areas. Hence, we combined the A2D and S1A deformation maps to retrieve the near-east and vertical components of the InSAR displacement.

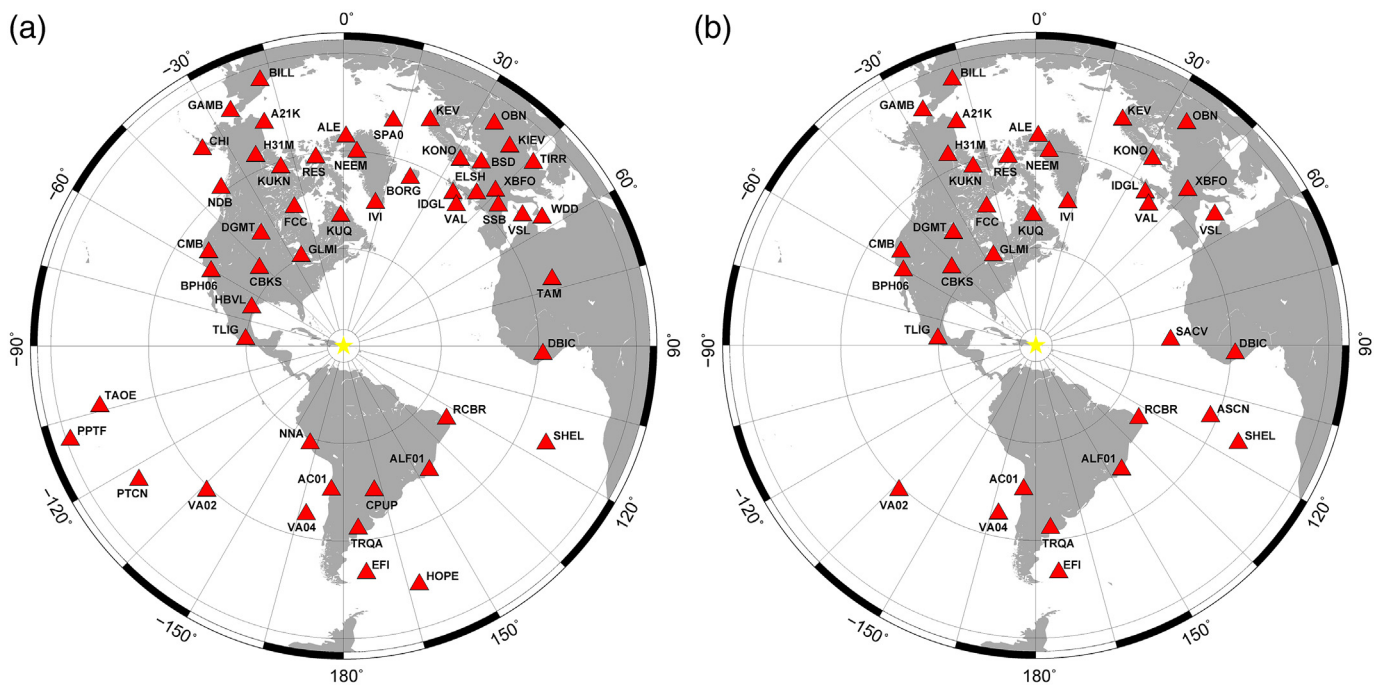
GNSS

We analyzed observations from 17 continuous GNSS stations belonging to the Puerto Rico's geodetic network (See [Data and Resources](#); Fig. 1). The GNSS observables span the time window from 1 January 2019 to 31 July 2020 are sampled at 30 s interval and stored into 24 hr session files. We used the GAMIT/GLOBK analysis software ([Herring et al., 2018](#)) to produce daily station position time series and hourly total zenith delay estimates during the GNSS observation time span. These estimates provide independent constraints on the coseismic deformation associated with the main events of the earthquake sequence and the APS, respectively.

The GNSS measurements were analyzed following the first two steps described by [Floyd et al. \(2010\)](#) and [Kogan et al. \(2012\)](#). In the first step, loosely constrained station positions and their associated covariances were estimated from the raw GNSS observations using precise satellite orbits and Earth's orientation parameters. This step included 18 additional IGS fiducial stations used to align the network's daily solutions to the ITRF2014 (defined after [Altamimi et al., 2017](#)). In the second step, final station positions in the ITRF2014 reference frame were obtained from combining the loosely constrained daily solutions using the GLOBK Kalman filter (See [Herring et al., 2018](#), for details). The reference frame was established by estimating a 6 parameter Helmert transformation constraining the positions of the 18 fiducial IGS stations to their ITRF2014 values. Finally, we combined the network's global daily solutions into GNSS position time series. After time series generation, outliers were removed using the $3 - \sigma$ rule, and the coseismic offsets were estimated by fitting a trajectory model that includes a linear trend and Heaviside step function terms at the dates of the earthquake sequence main events (equation 1):

$$P(t) = a + b \times t + c_i \times \sum_{i=1}^n H(t - t_i) + \epsilon(t). \quad (1)$$

This trajectory model describes well the GNSS time series for all the stations except two (P780 and PRMI), which required an additional exponential term to describe signals suggesting postseismic deformation. The character of the noise within the GNSS time series was included in the model parameter estimation using a linear combination of white and flicker components with the Hector software package ([Bos et al., 2013](#)). The median error for the GNSS-derived coseismic offsets is 1.2 mm for the horizontal and 3.2 mm for the vertical components, respectively. Details on the total zenith delay



estimation are presented in the supplemental material (Text S1; Figs. S1b, S2b, S3b).

Seismic data

The waveform data we used in the source parameter estimation come from seismic stations located at teleseismic distances within a range of 30°–90° from the earthquake location reported in the United States Geological Survey catalog ([University of Puerto Rico, 1986](#); Fig. 3). We selected 51 *P* and 35 *SH* waveforms providing the best signal-to-noise ratio and azimuthal coverage from seismic recordings accessed through the Incorporated Research Institutions for Seismology, the Geoforschungsnetz, and the Observatories & Research Facilities for European Seismology data centers (see [Data and Resources](#)). The raw waveforms were restituted to true ground displacement and rotated into the radial (*R*), transverse (*T*), and vertical (*Z*) components. The resulting waveforms were then bandpass-filtered from 100 s to 20 s to decrease effects associated with high-frequency noise ([Steinberg et al., 2020](#)).

For the model parameter inference (see the [Bayesian Inference of Earthquake Source Parameters](#) section), the vertical (*Z*) and transverse (*T*) components were used to fit the *P* and *SH* waveforms over a time window covering 10 s before and 60 s after the body- and surface-wave arrivals, respectively. To account for measurement and theory errors, we applied non-Toeplitz covariance matrices during the model parameter inference ([Dettmer et al., 2007](#); [Vasyura-Bathke et al., 2021](#)).

Bayesian inference of earthquake source parameters

We applied the Bayesian Theorem ([Bayes, 1763](#)) to infer the source parameters of the mainshock using the open-source

Figure 3. Locations of seismic stations providing the (a) 51 *P* and (b) 35 *SH* waveform recordings used in this study. The color version of this figure is available only in the electronic edition.

software BEAT ([Vasyura-Bathke et al., 2019, 2020](#)) using seismic waveforms and geodetic data from InSAR and GNSS, jointly. In the following, we use $\mathbf{d}_k^{\text{obs}}$ as variable for expressing a dataset k being a seismic waveform component at a station, a displacement field of an unwrapped interferogram in LOS, or the static offset of all GNSS stations for a displacement component.

Under the assumption of Gaussian distributed residuals $\mathbf{r}_k(\mathbf{m}) = \mathbf{d}_k^{\text{obs}} - \mathbf{d}_k(\mathbf{m})$ with $\mathbf{d}_k(\mathbf{m})$ being predicted synthetic data for dataset k , the posterior probability density of model parameters \mathbf{m} is given by

$$p(\mathbf{m}|\mathbf{d}^{\text{obs}}) \propto p(\mathbf{m}) \prod_{k=1}^K \frac{1}{(2\pi\sigma_k^2)^{N/2} |\mathbf{C}_k|^{1/2}} \exp\left[-\frac{1}{2\sigma_k^2} [\mathbf{r}_k(\mathbf{m})]^T \mathbf{C}_k^{-1} [\mathbf{r}_k(\mathbf{m})]\right], \quad (2)$$

for all datasets k . Here, \mathbf{C}_k is the covariance matrix describing the noise statistics of residual errors that are considered noise. We account for a hierarchical scaling σ_k to also estimate the standard deviation of the residuals. We then sample the posterior probability density using a sequential Monte Carlo algorithm ([Del Moral et al., 2006](#); [Vasyura-Bathke et al., 2020](#)), which is a special variant of Markov Chain Monte Carlo sampling.

We simulated synthetic static and transient displacements $\mathbf{d}_k(\mathbf{m})$ assuming a layered elastic halfspace using CRUST2 ([Bassin et al., 2000](#)) and AK135 ([Kennett et al., 1995](#)) for

the crustal and deeper Earth structures, respectively. To ensure numerical efficiency, we precalculated Green's Function stores (Heimann *et al.*, 2019). These Green's Functions are stored on a distance–depth grid and allow to create synthetics for any given source–receiver configuration. For the static data, we used PSGRN/PSCMP (software package dedicated to perform post-seismic Green's functions and post-seismic deformation computation) (Wang *et al.*, 2006) to calculate Green's Functions for a depth–distance range of 0–50 km and 0–500 km with half a kilometer spacing in both the directions. For the transient data, we used the quick seismograms for spherical earth models code (QSSP, Wang *et al.*, 2017) to calculate station-specific Green's Functions for a 1 km spacing grid extending laterally to 100 km around each station and covering a depth range of 0–25 km. All the Green's Functions were calculated relative to an arbitrary event reference location defined at 66.81° W and 18.08° N.

For the model parameter sampling, the full-resolution InSAR deformation fields were reduced to their statistically significant fractions following the 2D quantization algorithm (Jónsson *et al.*, 2002). We thus decreased the number of data points from millions to 59 for S1A, 57 for S1D, and 76 for A2D (Fig. S5). Then, data-specific covariance matrices were estimated following the method in Sudhaus and Jónsson (2009). Before downsampling, the orbital ramp and offset components described in the InSAR section were added back to the InSAR data and were re-estimated together with the source fault parameters. This allowed to use the derived covariance matrices as data weighting in the model parameter estimation.

For the seismic data, on the other hand, we estimated station-specific time shifts during the optimization to account for phase shifts resulting from velocity model uncertainties (Mustać *et al.*, 2020; Vasyura-Bathke *et al.*, 2021). Finally, only GNSS-derived horizontal coseismic offsets were used in our optimization, considering the distance from the geodetic network to the locus of vertical deformation and the better performance of the GNSS measurements in resolving for horizontal motions (e.g., Dixon, 1991; Floyd *et al.*, 2010; and references therein).

Results

Coseismic ground deformation

The interferograms time span cover several days of the seismic sequence (Fig. 2d), and, therefore, the InSAR-derived coseismic displacements are affected by all the events nucleating within the SAR acquisition time frames. However, all the InSAR-derived deformation maps show localized coseismic displacements around the Guayanilla bay (Fig. 4). On the western part of the bay, the LOS displacements indicate movements away from the satellite for the three looking geometries, suggesting that the majority of the deformation is along the vertical direction. However, the maximum displacement in the S1A (−14 cm) is smaller than that in the S1D and A2D (−23 and −26 cm, respectively), indicating a significant horizontal displacement

component as well. The eastern part of the bay moved toward the satellite for the S1A (5 cm) and away for the S1D and A2D (−17 and −19 cm, respectively), indicating primarily westward horizontal motions. This is confirmed by the InSAR-derived near-east and near-vertical ground displacement components (Fig. 5), showing that the entire bay subsided and moved westward with the maximum vertical (27 cm) and horizontal (20 cm) displacements on its western and eastern parts, respectively. The near-vertical displacement field also shows two uplifting areas flanking the Guayanilla bay (Fig. 5b), suggesting an additional component of northward motion, consistent with normal faulting along a east–west oriented fault dipping inland. Furthermore, the near-east displacement field (Fig. 5a) shows ~9 cm of relative motion in the Punta Brea area, consistent with left-lateral strike-slip faulting along the NBBPM fault.

Most of the GNSS stations of the Puerto Rico geodetic network are distant from the region of maximum displacement highlighted by InSAR, with only three sites (PRMI, PRGY, and P780) located within 10 km from the Guayanilla bay. However, away from the bay, where small coseismic deformations are expected, they provide more reliable estimates than InSAR. In addition, the daily solutions provide better constraints on the coseismic offsets compared with the InSAR-based displacements. The GNSS-derived coseismic offsets indicate horizontal motions mostly in the western half of the island reaching up to ~4.2 cm near the Guayanilla bay and ~0.8 cm at distances over ~65 km from the region of maximum deformation (Fig. 6). Their azimuths show a direction shift from southwest to northwest oriented roughly east and west of the earthquake's longitude, respectively (Fig. 6). This deformation pattern is consistent with a northward dipping normal fault with a significant left-lateral strike-slip component, as previously suggested by the InSAR-based deformation maps (Fig. 5). Their small magnitudes and azimuths lying at close angles from the SAR satellites' heading directions may explain why they are not well resolved by InSAR.

The cross validation of the GNSS- and InSAR-derived coseismic displacements indicate consistency between the independently derived datasets (Fig. S4), except at few coastal stations (e.g., EMPR, PRAR, PRLP, PRLT). This implies that the applied corrections removed most of the artifacts in the InSAR deformation maps, with the remnant noise probably associated with the local atmospheric signals.

Source model

The source model used to assess the main event of the 2019–2020 Puerto Rico earthquake sequence considers uniform slip on a single rectangular fault embedded in a layered elastic half-space. The model setup responds to the large amount of seismic energy released by the mainshock as well as the presence of several indistinguishable aftershocks within the geodetic data. All the source fault parameters were loosely constrained before sampling; however, the priors defining the location, orientation, and

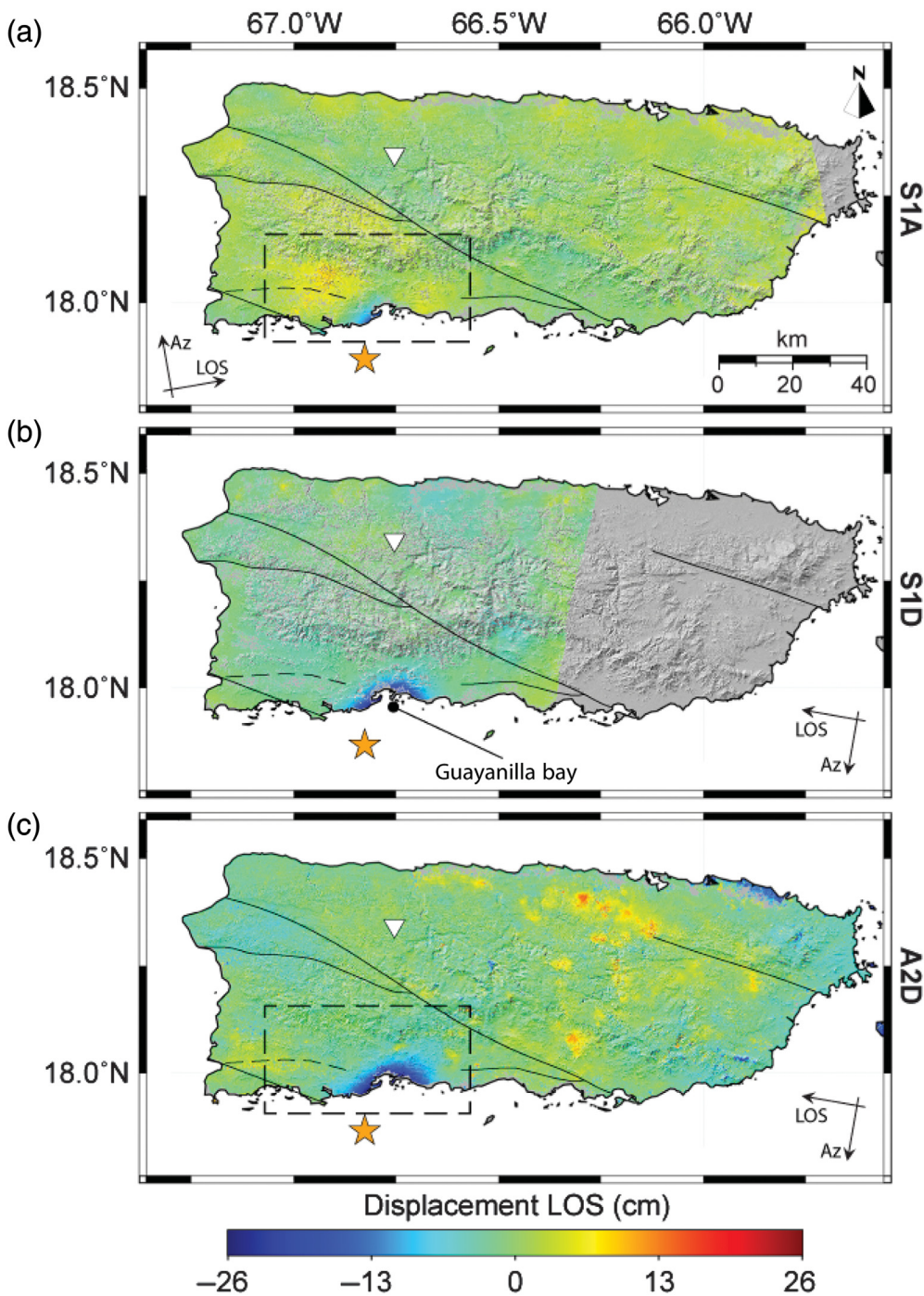


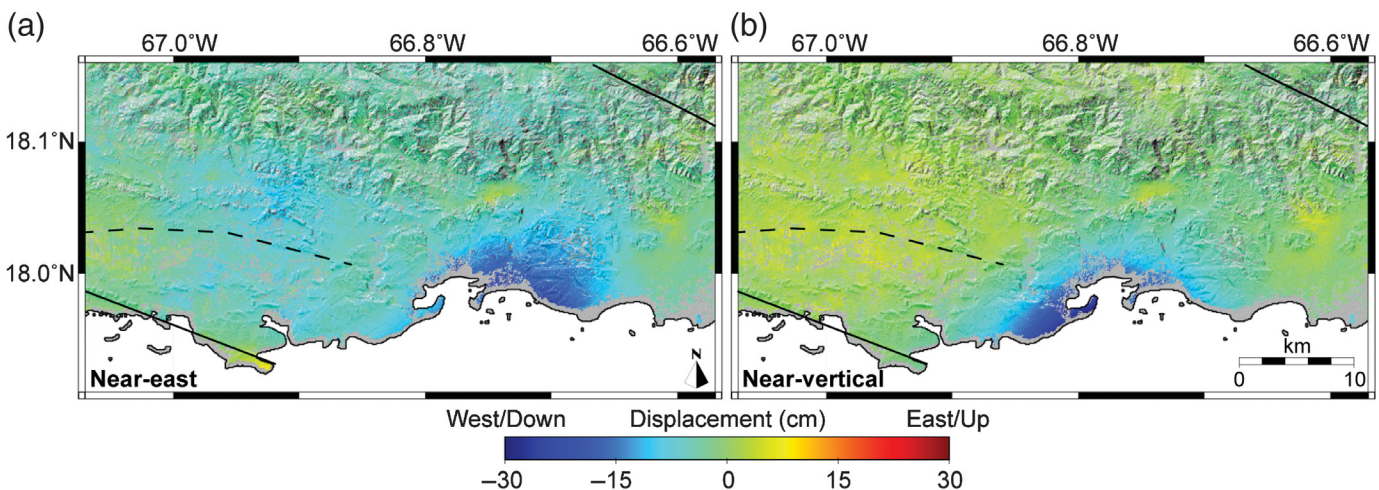
Figure 4. Unwrapped Interferometric SAR (InSAR) images from (a) ascending and (b) descending Sentinel-1 (SA1 and S1D), and (c) descending ALOS-2 (A2D) data. Black boxes in panels (a) and (c) outline the area shown in Figure 5. The orange star marks the sequence's mainshock location by University of Puerto Rico, 1986. Arrows indicate the satellites' heading (AZ) and the looking (LOS) directions, respectively. The inverted white triangle is the reference point for the unwrapping and corresponds to the AOPR GNSS station. Black lines are the main faults.

faulting style include information from the focal mechanism reported by the University of Puerto Rico (1986). The source fault parameters were sampled in 33 stages, in which the forward model was evaluated ~ 10 million times.

due to stronger residual noise still present in the deformation map, particularly at distances between 18 and 30 km from the coast. The MAP fault parameters explain all the GNSS-derived horizontal coseismic offsets within the 95% uncertainty level of

The combination of model parameters (along with the 0.5 and 99.5 percentiles) with the maximum likelihood of explaining the three datasets simultaneously results in a $12.5_{-0.7}^{+2.2}$ km long and $9.7_{-1.0}^{+1.2}$ km wide (between $5.9_{-0.6}^{+0.3}$ and $12.9_{-1.1}^{+1.3}$ km of depth) fault accommodating $\sim 1.4_{-0.3}^{+0.1}$ m of fault slip (Fig. 7). The fault strikes at $273.0_{-0.9}^{+1.3}$ and dips toward the Guayanilla bay at an angle of $46.8_{-0.3}^{+1.0}$ (Figs. 7 and 8). The estimated rake angle ($-47.2_{-1.1}^{+0.6}$) indicates a combination of roughly equal normal and left-lateral strike-slip faulting components. By assuming a constant rupture velocity of 3.5 km/s and a half-sinusoidal source time function, we estimated that the rupture nucleated in the lower east quadrant of the fault and propagated up- and westward for $10.6_{-0.4}^{+0.5}$ s. The seismic moment associated to the modeled fault is 5.1×10^{18} Nm, consistent with the reported $M_w 6.4$ earthquake. The model parameters with the maximum a posteriori probability (MAP) are shown in Figure 7.

The predicted coseismic displacements projected into the LOS direction of the three SAR geometries can explain $\sim 61\%$ of the observed InSAR signal (Fig. 8). The resulting modeled ground deformation for the S1D and A2D is comparable due to their similar acquisition geometries; however, the maximum displacements are underestimated for A2D (Fig. 8). The cross section in Figure 8j supports this outcome and shows the poorer fit to the S1A data



the dataset, except for the PRGY and PRMI stations (Fig. 6). In both the cases, the predicted directions depart from the observations, whereas the magnitude is overestimated for PRMI and slightly underestimated for PRGY, respectively. This discrepancy could result from local displacements associated with an aftershock nucleating within the same day of the mainshock and, therefore, aliased in the offset estimate.

The weighted variance reduction for the teleseismic waveforms indicate a better fit to the vertical (P waves) than to the transversal (S waves) component data (Fig. 9). Moreover, the

Figure 5. (a) Near-east and (b) near-vertical displacements derived from the combination of the Sentinel-1 ascending (SA1) and ALOS-2 (A2D) deformation maps (Fig. 4b,c).

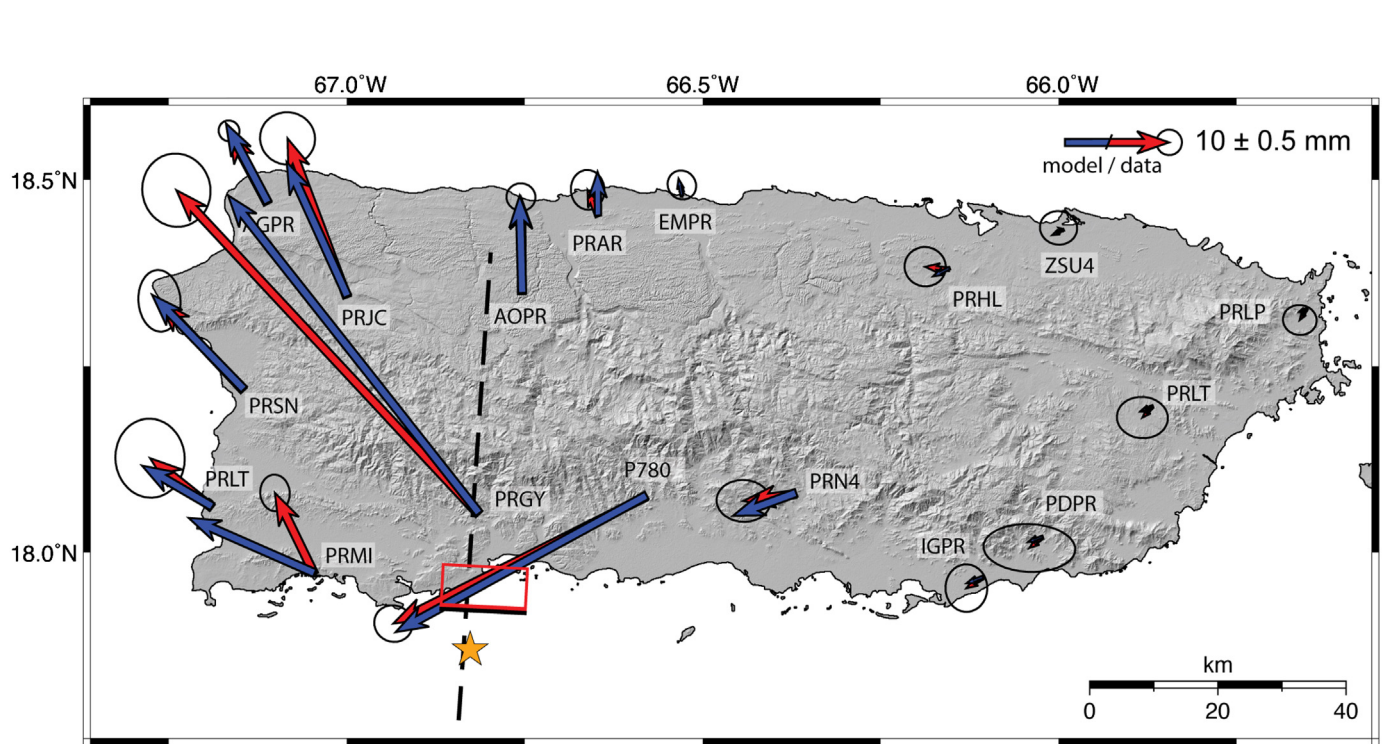
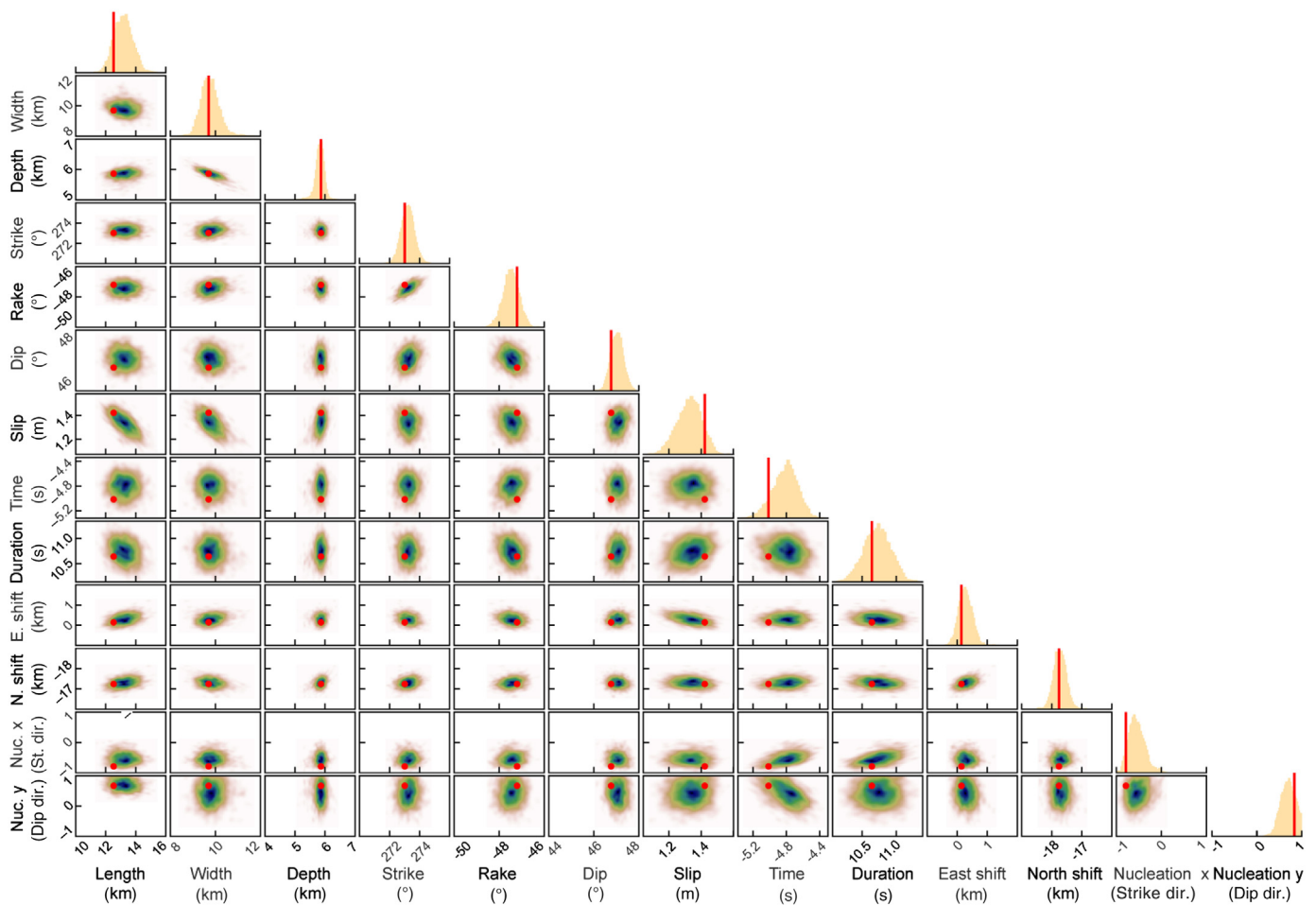


Figure 6. Observed (red arrows) and predicted (blue arrows) horizontal coseismic offsets by the source fault parameters with the maximum a posteriori probability (MAP) at the GNSS station locations. Ellipses show the 95% confidence interval of the horizontal coseismic offsets. The red box shows the surface

projection of the MAP source fault with the solid-black line indicating the upper edge. Dashed-black line marks the full extent of the profile shown in Figure 8. The color version of this figure is available only in the electronic edition.



Discussion

Both the alignments and focal mechanisms of earthquakes during the 2020 southwest Puerto Rico seismic sequence indicate activation of different fault segments and secondary faults located both inland and offshore (Fig. 2a–c). This is further supported by the horizontal displacements derived from the InSAR deformation maps on the southernmost La Brea peninsula, indicating up to ~ 9 cm of eastward motion, consistent with left-lateral strike-slip faulting (Fig. 5). The aforementioned, in combination with the spatial distribution of events (~ 50 km long and ~ 30 km wide east–west oriented area), suggest a diffuse rather than a sharp boundary accommodating the Caribbean–PR–VI relative motion (e.g., Jansma *et al.*, 2000; Jansma and Mattioli, 2005; Prentice and Mann, 2005). Moreover, the magnitude of the main event and the large number of moderate aftershocks suggest a high coupling of the fault system, consistent with the expected strain partitioning resulting from oblique convergence in the area, as previously proposed by Jansma *et al.* (2000) and Jansma and Mattioli (2005).

Using a conceptual physical model for permeability dynamics in the crust, Miller (2020) demonstrated that long-duration and rich-aftershock sequences are expected at zones of dilatation that have limited tectonic ability to reseal

Figure 7. One-dimensional and 2D marginal posteriors for the fault source model parameters constrained by combination of the GNSS, InSAR, and teleseismic data. The red vertical lines in the histograms and the red dot in the 2D correlation plots mark the MAP solution. In the correlation plots, blue colors are regions of high probability. East and North shifts are relative to the reference location defined in the [Bayesian Inference of Earthquake Source Parameters](#) section. The color version of this figure is available only in the electronic edition.

the co- and postseismically generated fracture networks. On this basis, a complex evolution dominated by fluid-driven earthquakes resulting from pore pressure diffusion was proposed for the 2020 southwest Puerto Rico seismic sequence, which occurred within a transtensional tectonic regime with potentially abundant deep fluid sources (e.g., Peacock, 1990; Jansma and Mattioli, 2005). The previous interpretation is further supported by the fact that the largest event of the seismic sequence (M_w 6.4) accounted for only $\sim 60\%$ of the total seismic energy released (e.g., University of Puerto Rico, 1986).

The MAP fault parameters of the 7 January 2020 M_w 6.4 Puerto Rico earthquake indicate normal faulting with a left-lateral strike-slip component on a roughly east–west oriented, northward-dipping fault offshore the Guayanilla bay (Figs. 6

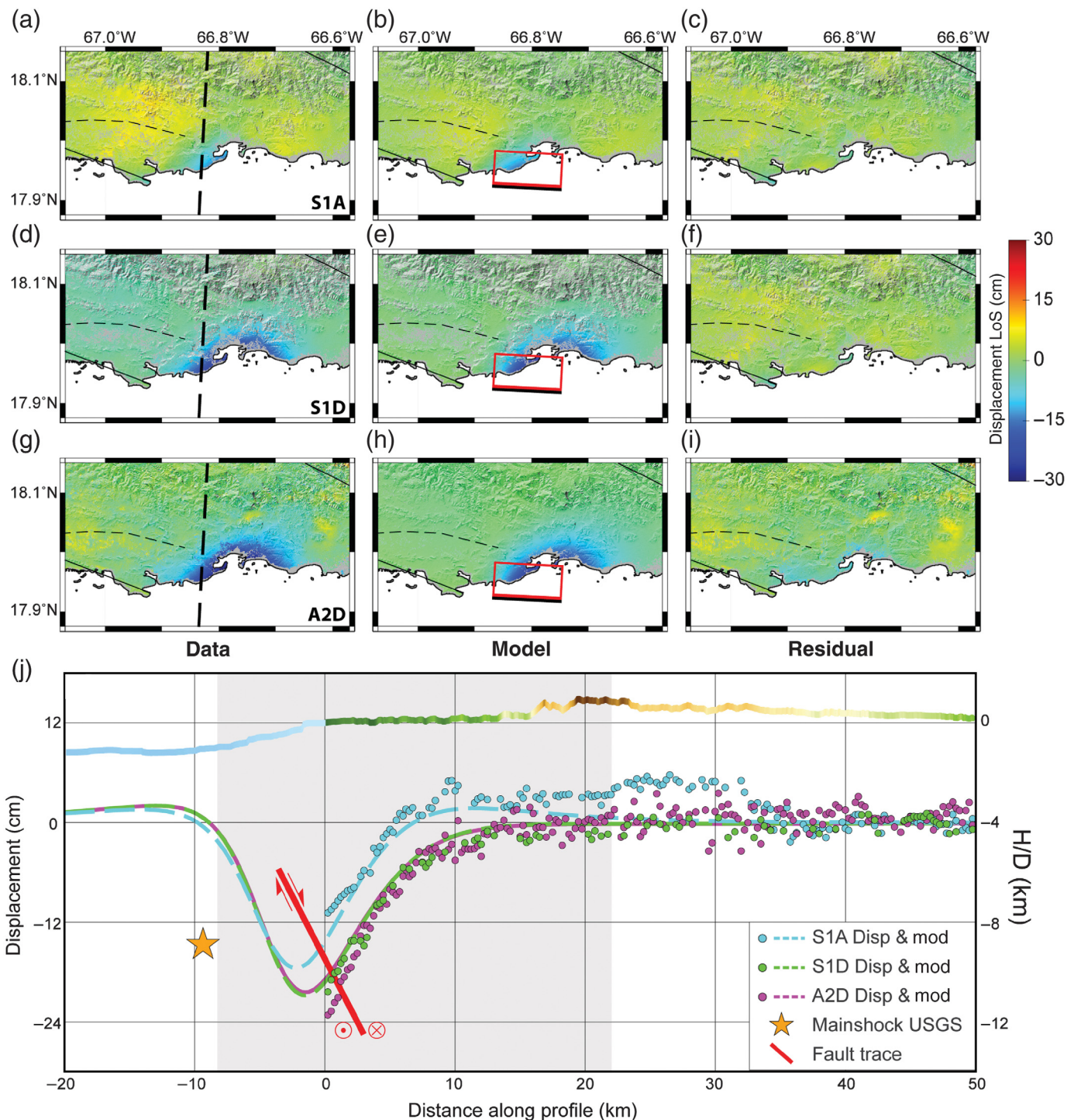


Figure 8. (a,d,g) Zoom on the area affected by the largest coseismic displacement (around Guayanilla bay) for the S1A, S1D, and A2D deformation maps, respectively. The thick dashed lines mark the cross sections shown in panel (j). (b,e,h) Predicted line-of-sight (LOS) displacements for each orbit. The red box is the surface projection of the MAP source fault with the black line indicating the top. (c,f,i) The residual LOS displacements.

(j) A cross section of the topography and bathymetry (plotted according to a different colorscale), the MAP source fault (red), along with the observed (circles) and predicted (dashed lines) LOS displacements profiles for the S1A (cyan), S1D (green), and A2D (magenta) orbits, respectively. Orange star depicts the sequence's mainshock location ([University of Puerto Rico, 1986](#)).

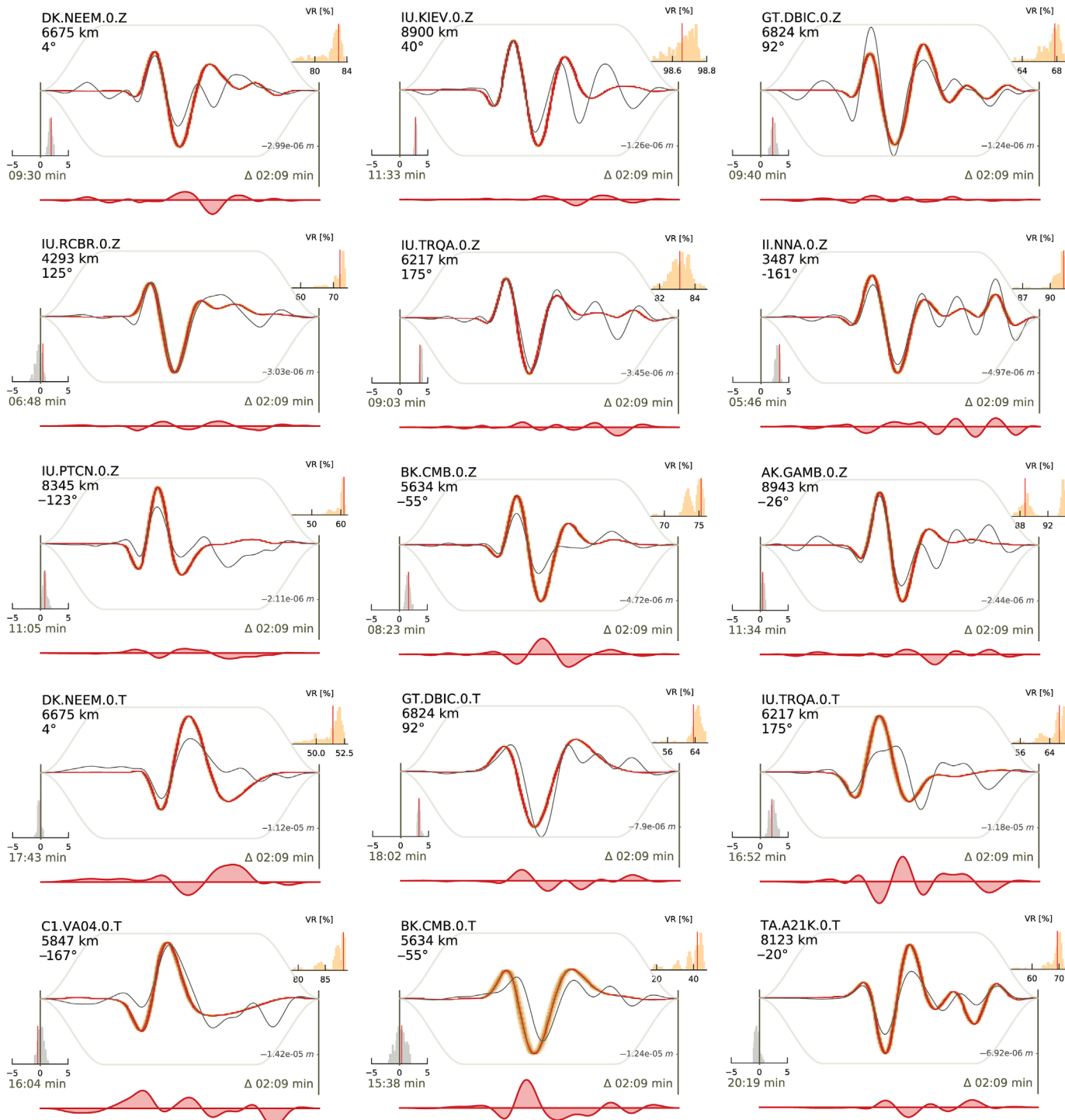
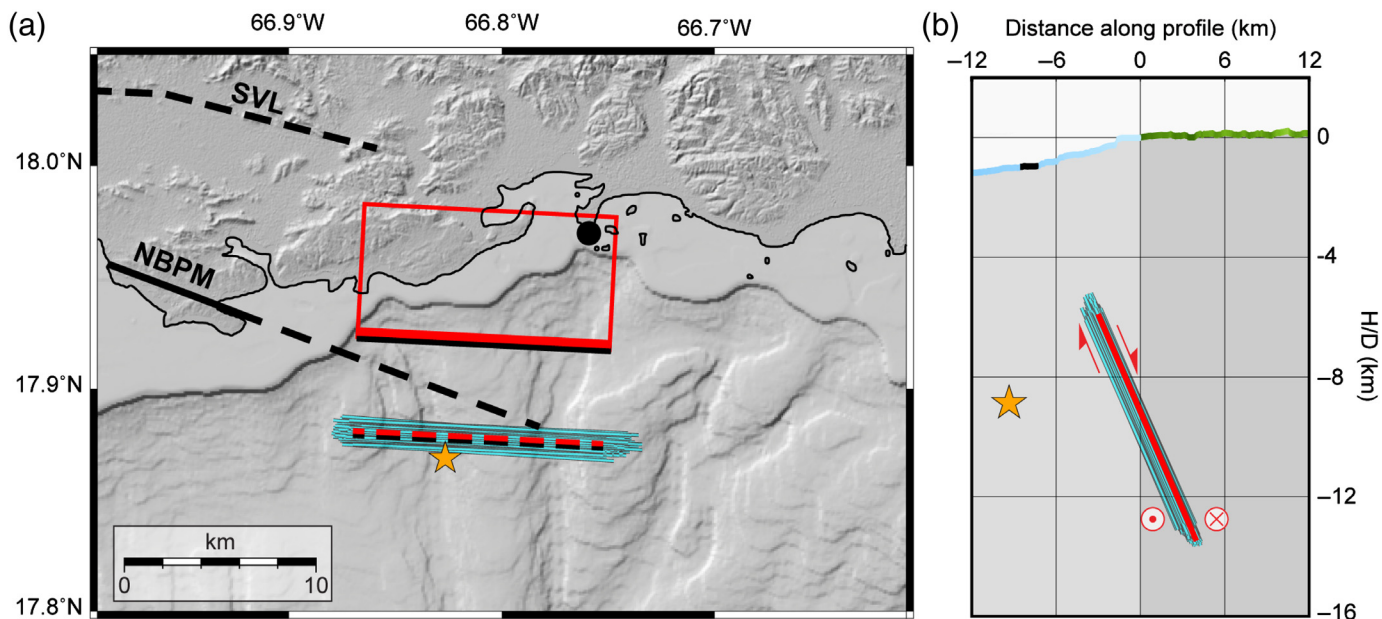


Figure 9. Waveform fits at selected seismic stations for nine body (top) and six surface (bottom) wave seismic recordings. Gray- and red-solid lines depict the filtered (0.01–0.05 Hz) observed and synthetic displacement waveforms respectively. The brown shading shows 200 randomly selected synthetic waveforms from the posterior predictive distribution. Red lines with filled polygons show the residual waveforms. Traces are annotated with station name, component, epicentral distance, and azimuth from the

center of the MAP source fault. The arrival time and the duration of each window are shown in the lower left and right, respectively. The gray and orange histograms on the lower left and top right corners of each plot show the station-specific time shift and the weighted variance reduction (VR) for the posterior predictive distribution, respectively. The color version of this figure is available only in the electronic edition.



and 8). The predicted displacements around the bay represent about two-thirds of the InSAR-derived deformation fields, in agreement with the ratio of mainshock to aftershock seismic energy release (e.g., University of Puerto Rico, 1986). Furthermore, the fault orientation (strike, dip) and slip direction (rake) are consistent with patterns of strain accumulation estimated for southwestern Puerto Rico (e.g., Huérfano *et al.*, 2005; Jansma and Mattioli, 2005).

Our estimated strike, dip, and rake angles are $\sim 6^\circ$, $\sim 4^\circ$, and $\sim 11^\circ$ larger, respectively, than the solutions from the University of Puerto Rico (1986) and Liu *et al.* (2020). Likewise, the depth of our estimated nucleation point (~ 12 km) is slightly larger than the hypocentral depth reported by the University of Puerto Rico (1986). However, our fault location parameters (north and east shift; Fig. 7) imply a northward shift of ~ 18 km toward the Guayanilla bay, consistent with the hypocenter relocation derived from regional seismic data by Liu *et al.* (2020; Figs. 6 and 8j). The rupture time yielded by our analysis (~ 11 s) is almost 3 times longer than reported by the University of Puerto Rico (1986), but is in good agreement with the Liu *et al.* (2020) results (~ 11 s). The difference with respect to the University of Puerto Rico (1986) estimate may result from non-double-couple seismic energy being radiated in response to fault complexities like bending and change of dip angle with depth. Alternatively, it may indicate fault rupture within a soft material with relatively low shear-wave velocity.

Drawing 1200 random samples of the source fault indicates that its surface trace intercepts with a straight continuation of the NBBPM fault (Fig. 10), suggesting that either the mainshock ruptured along a subparallel planar fault south of the NBBPM fault, or both the strike and dip of the latter fault changes as it gets offshore. The presence of several offshore east–west trending faults in southwestern Puerto Rico (e.g., Grindlay *et al.*, 2005) and the strain partitioning between

Figure 10. Fault trace along the (a) strike and (b) dip directions obtained by drawing 1200 random source fault samples. Black dot depicts the earthquake nucleation point. Fault surface projection is represented as in Figure 6. Orange star depicts the sequence's mainshock location by University of Puerto Rico, 1986. The color version of this figure is available only in the electronic edition.

left-lateral strike-slip and compression inferred from earthquake focal mechanisms in the southeast of the Lajas Valley (Roig-Silva *et al.*, 2013; Fig. 2a, b) support fault bending along the strike direction around the Guayanilla bay area. Moreover, onland shallow seismicity on the eastern part of the NBBPM fault indicates mostly subvertical fault planes (e.g., Huérfano *et al.*, 2005), supporting the proposed changes in dip angle with depth and likely explaining our estimated relatively long rupture time. Based on the earlier information, we postulate that the 7 January 2020 M_w 6.4 Puerto Rico earthquake likely nucleated on an offshore continuation of the NBBPM fault, which bends northward and changes dip with depth as it runs beneath the Guayanilla bay.

Despite the intensive microseismicity, neither instrumental nor historical major earthquakes have been localized in this area (e.g., University of Puerto Rico, 1986; Huérfano *et al.*, 2005; Prentice and Mann, 2005; Clinton *et al.*, 2006). However, onshore paleoseismic trenching indicate Holocene surface ruptures requiring magnitude 6 or greater earthquakes in southwestern Puerto Rico (e.g., Prentice and Mann, 2005). Kinematic models constrained by GNSS-derived velocities suggest that internal deformation within the PR-VR microplate falls below the uncertainty level of the observations (~ 0.5 mm/yr; Symithe *et al.*, 2015). Yet, differential motions between GNSS stations in southwestern Puerto Rico reach 1–2.3 mm/yr (ten Brink and López-Venegas, 2012; Yang *et al.*, 2016; Wang *et al.*, 2019). Projecting these values onto our

modeled source fault yields a recurrence time ranging from \sim 700 to \sim 1500 yr for the nucleation of an earthquake of similar magnitude within this diffuse plate boundary in southwestern Puerto Rico. These values, however, provide lower bounds of the earthquake cycle recurrence time, because a single fault is assumed to accommodate all the relative motion.

The lack of near-field measurements combined with geodetic observations being limited to the hangingwall, prevents solving for the distributed slip on the source fault. We considered several model scenarios using different fault discretizations and parameter sampling approaches including: 1) user-defined fault patch sizes, 2) resolution-based discretization following the method described by Atzori and Antonioli (2011), 3) Laplacian smoothing weights, and 4) velocity model variations. However, in every case, this resulted in over-parameterization of the fault plane, with only marginal improvements of the variance reduction.

Together with the former parameter sampling scenarios, we performed sensitivity tests to address the influence of each individual dataset in the MAP parameter results (Figs. S6–S9). Using only the InSAR data for the parameter inference resulted in a fault oriented in an oblique direction relative to the fault obtained from combination of the three datasets, consistent with the presence of northeast–southwest oriented aftershocks within the SAR acquisitions (Figs. 2; Fig. S7). The GNSS data alone appears to constrain well the fault orientation, but they provides limited constraint to the fault slip and geometry (Fig. S8). These tests highlight the need for combination of independent datasets when estimating earthquake source parameters, because explaining well a single dataset may result in biased parameter estimates due to the lack of data (Salichon *et al.*, 2003; Delouis *et al.*, 2010). This is particularly important in our case, because most of the coseismic surface displacements occurred offshore and, therefore, are missing in the geodetic data.

Conclusions

We combined InSAR, GNSS, and teleseismic waveforms to constrain the source fault parameters of the 7 January 2020 M_w 6.4 Puerto Rico earthquake using Bayesian inference. The location and orientation parameters yield an offshore blind fault, striking roughly east–west and dipping northward below the Guayanilla bay in southwestern Puerto Rico. Our results suggest that an offshore continuation of the NBBPM fault zone could have generated the earthquake. Still, the aftershocks distribution and focal mechanisms evidence a complex fault network in southwest Puerto Rico, accommodating the relative plate motion along a diffuse rather than sharp boundary (e.g., Prentice and Mann, 2005). The slip direction implies normal faulting with a left-lateral strike-slip component, consistent with transtensional patterns of strain accumulation in the area (e.g., Jansma and Mattioli, 2005). Together, the results indicate transtensional faulting in southwestern Puerto Rico in response to

active diffuse deformation affecting the PR–VI microplate, and highlight the existence of unmapped faults with moderate-to-large earthquake potential in the Puerto Rico region.

Data and Resources

Global Navigation Satellite System (GNSS) daily files from the Puerto Rico's geodetic network were obtained through the National Oceanic and Atmospheric Administration's (NOAA's) Continuously Operating Reference Stations database available at <ftp://geodesy.noaa.gov/cors/> (last accessed September 2020). Sentinel-1 images were obtained from the European Space Agency (ESA) through the Alaska Vertex facility available at <https://search.asf.alaska.edu/> (last accessed February 2020). The ALOS-2 images were provided by the Japan Aerospace Exploration Agency (JAXA) within the projects ER2A2N016 and ER2A2N161. Earthquake locations and focal mechanisms were downloaded from the United States Geological Survey catalog available at <https://earthquake.usgs.gov/earthquakes/search/> (last accessed January 2021). Digital elevation model (DEM) and bathymetry data were downloaded from <https://topex.ucsd.edu/> (last accessed February 2020). Fault traces shown in the plots were obtained from the CCAF-DB: the Caribbean and Central American active fault database https://github.com/GEMScienceTools/central_am_carib_faults (last accessed August 2020). Teleseismic waveforms were obtained from the Incorporated Research Institutions for Seismology (IRIS; <https://www.iris.edu>, last accessed October 2020), Geoforschungsnetz (GEOFON) (<https://geofon.gfz-potsdam.de/waveform/>, last accessed October 2020), and Observatories & Research Facilities for European Seismology (ORFEUS; <https://www.orfeus-eu.org/data/>, last accessed October 2020) data centers, respectively. The GNSS and Interferometric Synthetic Aperture Radar (InSAR) data were processed with the GAMIT/GLOBK (<http://geoweb.mit.edu/gg/>, last accessed September 2020) and GAMMA (<https://www.gamma-rs.ch/>, last accessed March 2020) software packages, respectively. Model parameter sampling was performed using the Bayesian Earthquake Analysis Tool (BEAT; <https://github.com/hvasbath/beat>, last accessed April 2021). All plots in this article were produced using the Generic Mapping Tools version 5.4.4 and the Python plotting library Matplotlib. The supplemental material for this article includes nine figures supporting four sections depicted to provide detailed information on the corrections applied to the InSAR-derived deformation fields, cross validation between the GNSS- and InSAR-derived coseismic deformation, the downsampling of the InSAR deformation maps, and the data-specific sensitivity tests performed in this study.

Declaration of Competing Interests

The authors acknowledge that there are no conflicts of interest to report.

Acknowledgments

This research was supported by the King Abdullah University of Science and Technology (KAUST), under the Award Number BAS/1/1353-01-01. The authors are grateful to P. Martin Mai, Luigi Passarelli, and Yann Klinger for their insightful suggestions to our article. They also thank the Seismological Research Letters Editor-in-Chief Allison Bent and two anonymous reviewers for constructive comments that significantly improved this article. The

ALOS-2 images were provided by the Japan Aerospace Exploration Agency (JAXA) within the projects ER2A2N016 and ER2A2N161.

References

- Adames-Corraliza, A. R. (2017). Geomorphic and geophysical characterization of the north Boquerón Bay-Punta Montalva fault zone: A capable fault system in southwestern Puerto Rico, Unpublished master's thesis, Department of Geology, University of Puerto Rico, available at <https://hdl.handle.net/20.500.11801/856> (last accessed August 2021).
- Altamimi, Z., L. Miétivier, P. Rebischung, H. Rouby, and X. Collilieux (2017). ITRF2014 plate motion model, *Geophys. J. Int.* **209**, no. 3, 1906–1912, doi: [10.1093/gji/ggx136](https://doi.org/10.1093/gji/ggx136).
- Atzori, S., and A. Antonioli (2011). Optimal fault resolution in geodetic inversion of coseismic data, *Geophys. J. Int.* **185**, no. 1, 529–538, doi: [10.1111/j.1365-246X.2011.04955.x](https://doi.org/10.1111/j.1365-246X.2011.04955.x).
- Bassin, C., G. Laske, and G. Masters (2000). The current limits of resolution for surface wave tomography in North America, *EOS Trans. AGU* **81**, no. 48, F897.
- Bayes, T. (1763). An essay towards solving a problem in the doctrine of chances, *Philos. Trans.* **53**, 370–418.
- Bos, M. S., R. M. S. Fernandes, S. D. P. Williams, and L. Bastos (2013). Fast error analysis of continuous GNSS observations with missing data, *J. Geod.* **87**, no. 4, 351–360, doi: [10.1007/s00190-012-0605-0](https://doi.org/10.1007/s00190-012-0605-0).
- Calais, E., A. Freed, G. Mattioli, F. Amelung, S. Jónsson, P. Jansma, and R. Momplaisir (2010). Transpressional rupture of an unmapped fault during the 2010 Haiti earthquake, *Nat. Geosci.* **3**, no. 11, 794–799, doi: [10.1038/ngeo992](https://doi.org/10.1038/ngeo992).
- Calais, E., S. Symithe, B. Mercier de Liépinay, and C. Prépetit (2016). Plate boundary segmentation in the northeastern Caribbean from geodetic measurements and Neogene geological observations, *C. R. Geosci.* **348**, no. 1, 42–51, doi: [10.1016/j.crte.2015.10.007](https://doi.org/10.1016/j.crte.2015.10.007).
- Cheng, S., D. Perissin, H. Lin, and F. Chen (2012). Atmospheric delay analysis from GPS meteorology and InSAR APS, *J. Atmos. Sol. Terr. Phys.* **86**, 71–82, doi: [10.1016/j.jastp.2012.06.005](https://doi.org/10.1016/j.jastp.2012.06.005).
- Clinton, J. F., G. Cua, V. Huérano, C. G. von Hillebrandt-Andrade, and J. M. Cruzado (2006). The current state of seismic monitoring in Puerto Rico, *Seismol. Res. Lett.* **77**, no. 5, 532–543, doi: [10.1785/gssrl.77.5.532](https://doi.org/10.1785/gssrl.77.5.532).
- Dalla Via, G., M. Crosetto, and B. Crippa (2012). Resolving vertical and east-west horizontal motion from differential interferometric synthetic aperture radar: The L'Aquila earthquake, *J. Geophys. Res.* **117**, no. B2, doi: [10.1029/2011JB008689](https://doi.org/10.1029/2011JB008689).
- Del Moral, P., A. Doucet, and A. Jasra (2006). Sequential Monte Carlo samplers, *J. Royal Stat. Soc. B* **68**, no. 3, 411–436.
- Delouis, B., D. Giardini, P. Lundgren, and J. Salichon (2002). Joint inversion of InSAR, GPS, teleseismic, and strong-motion data for the spatial and temporal distribution of earthquake slip: Application to the 1999 Izmit mainshock, *Bull. Seismol. Soc. Am.* **92**, 278–299.
- Delouis, B., J.-M. Nocquet, and M. Vallée (2010). Slip distribution of the February 27, 2010 Mw = 8.8 Maule earthquake, central Chile, from static and high-rate GPS, InSAR, and broadband teleseismic data, *Geophys. Res. Lett.* **37**, no. 17, doi: [10.1029/2010GL043899](https://doi.org/10.1029/2010GL043899).
- DeMets, C., P. E. Jansma, G. S. Mattioli, T. H. Dixon, F. Farina, R. Bilham, and P. Mann (2000). GPS geodetic constraints on Caribbean-North America plate motion, *Geophys. Res. Lett.* **27**, no. 3, 437–440, doi: [10.1029/1999GL005436](https://doi.org/10.1029/1999GL005436).
- Dettmer, J., S. E. Dosso, and C. W. Holland (2007). Uncertainty estimation in seismoacoustic reflection travel time inversion, *J. Acoust. Soc. Am.* **122**, no. 1, 161–176, doi: [10.1121/1.2736514](https://doi.org/10.1121/1.2736514).
- Dixon, T. H. (1991). An introduction to the global positioning system and some geological applications, *Rev. Geophys.* **29**, no. 2, 249–276, doi: [10.1029/91RG00152](https://doi.org/10.1029/91RG00152).
- Farr, T. G., and M. Kobrick (2000). Shuttle radar topography mission produces a wealth of data, *EOS Trans. AGU* **81**, no. 48, 583–585, doi: [10.1029/EO081i048p00583](https://doi.org/10.1029/EO081i048p00583).
- Fielding, E. J., Z. Liu, O. L. Stephenson, M. Zhong, C. Liang, A. Moore, and M. Simons (2020). Surface deformation related to the 2019 Mw 7.1 and 6.4 Ridgecrest earthquakes in California from GPS, SAR interferometry, and SAR pixel offsets, *Seismol. Res. Lett.* **91**, no. 4, 2035–2046, doi: [10.1785/0220190302](https://doi.org/10.1785/0220190302).
- Floyd, M. A., H. Billiris, D. Paradissis, G. Veis, A. Avallone, P. Briole, J.-M. Nocquet, K. Palamarchouk, B. Parsons, and P. C. England (2010). A new velocity field for Greece: Implications for the kinematics and dynamics of the Aegean, *J. Geophys. Res.* **115**, no. B10, doi: [10.1029/2009JB007040](https://doi.org/10.1029/2009JB007040).
- Fuhrmann, T., and M. Garthwaite (2019). Resolving three-dimensional surface motion with InSAR: Constraints from multi-geometry data fusion, *Remote Sens.* **11**, no. 3, 241, doi: [10.3390/rs11030241](https://doi.org/10.3390/rs11030241).
- Goldstein, R. M., and C. L. Werner (1998). Radar interferogram filtering for geophysical applications, *Geophys. Res. Lett.* **25**, no. 21, 4035–4038, doi: [10.1029/1998GL900033](https://doi.org/10.1029/1998GL900033).
- Granja Bruña, J., U. ten Brink, A. Carbó-Gorosabel, A. Muñoz-Martín, and M. Gómez Ballesteros (2009). Morphotectonics of the central muertos thrust belt and muer- tos trough (northeastern caribbean), *Mar. Geol.* **263**, no. 1, 7–33, doi: [10.1016/j.margeo.2009.03.010](https://doi.org/10.1016/j.margeo.2009.03.010).
- Grindlay, N. R., P. Mann, J. F. Dolan, and J.-P. van Gestel (2005). Neotectonics and subsidence of the northern Puerto Rico-Virgin Islands margin in response to the oblique subduction of high-standing ridges, in *Active Tectonics and Seismic Hazards of Puerto Rico, the Virgin Islands, and Offshore Areas*, Geological Society of America, doi: [10.1130/0-8137-2385-X.31](https://doi.org/10.1130/0-8137-2385-X.31).
- Hanssen, R. (2001). *Radar Interferometry: Data interpretation and Error Analysis*, Vol. 2, Springer, Dordrecht, doi: [10.1007/0-306-47633-9](https://doi.org/10.1007/0-306-47633-9).
- Heimann, S., H. Vasyura-Bathke, H. Sudhaus, M. P. Isken, M. Kriegerowski, A. Steinberg, and T. Dahm (2019). A Python framework for efficient use of pre-computed Green's functions in seismological and other physical forward and inverse source problems, *Solid Earth* **10**, no. 6, 1921–1935, doi: [10.5194/se-10-1921-2019](https://doi.org/10.5194/se-10-1921-2019).
- Herring, T. A., R. W. King, M. A. Floyd, and S. C. McClusky (2018). Documentation for the GAMIT/GLOBK GNSS Analysis Software, release 10.7 [Computer software manual] Cambridge.
- Hudnut, K. W., Y. Bock, M. Cline, P. Fang, Y. Feng, J. Freymueller, X. Ge, W. K. Gross, D. Jackson, M. Kim, et al. (1994). Co-seismic displacements of the 1992 Landers earthquake sequence, *Bull. Seismol. Soc. Am.* **84**, no. 3, 625–645.
- Huérano, V., C. von Hillebrandt-Andrade, and G. Báez-Sánchez (2005). Microseismic activity reveals two stress regimes in southwestern Puerto Rico, in *Active Tectonics and Seismic Hazards of Puerto Rico, the Virgin Islands, and Offshore Areas*,

- P. Mann (Editor), Vol. 385, Geological Society of America, doi: [10.1130/0-8137-2385-X.81](https://doi.org/10.1130/0-8137-2385-X.81).
- Jansma, P. E., and G. S. Mattioli (2005). GPS results from Puerto Rico and the Virgin Islands: Constraints on tectonic setting and rates of active faulting, in *Active Tectonics and Seismic Hazards of Puerto Rico, the Virgin Islands, and Offshore Areas*, Geological Society of America, doi: [10.1130/0-8137-2385-X.13](https://doi.org/10.1130/0-8137-2385-X.13).
- Jansma, P. E., G. S. Mattioli, A. Lopez, C. DeMets, T. H. Dixon, P. Mann, and E. Calais (2000). Neotectonics of Puerto Rico and the Virgin Islands, northeastern Caribbean, from GPS geodesy, *Tectonics* **19**, no. 6, 1021–1037, doi: [10.1029/1999TC001170](https://doi.org/10.1029/1999TC001170).
- Jónsson, S., H. Zebker, P. Segall, and F. Amelung (2002). Fault slip distribution of the 1999 Mw 7.1 Hector Mine, California, earthquake, estimated from satellite radar and GPS measurements, *Bull. Seismol. Soc. Am.* **92**, no. 4, 1377–1389, doi: [10.1785/0120000922](https://doi.org/10.1785/0120000922).
- Kennett, B. L. N., E. R. Engdahl, and R. Buland (1995). Constraints on seismic velocities in the Earth from traveltimes, *Geophys. J. Int.* **122**, no. 1, 108–124, doi: [10.1111/j.1365-246X.1995.tb03540.x](https://doi.org/10.1111/j.1365-246X.1995.tb03540.x).
- Kogan, L., S. Fisseha, R. Bendick, R. Reilinger, S. McClusky, R. King, and T. Solomon (2012). Lithospheric strength and strain localization in continental extension from observations of the East African Rift, *J. Geophys. Res.* **117**, no. B3, doi: [10.1029/2011JB008516](https://doi.org/10.1029/2011JB008516).
- Konca, A. O., S. Leprince, J.-P. Avouac, and D. V. Helmberger (2010). Rupture process of the 1999 Mw 7.1 Duzce earthquake from joint analysis of SPOT, GPS, InSAR, strong-motion, and teleseismic data: A supershear rupture with variable rupture velocity, *Bull. Seismol. Soc. Am.* **100**, no. 1, 267–288, doi: [10.1785/0120090072](https://doi.org/10.1785/0120090072).
- Laó-Dávila, D. A., P. Mann, C. S. Prentice, and G. Draper (2000). Late Quaternary activity of the Cerro Goden fault zone, transpressional uplift of the La Cedena Range, and their possible relation to the opening of the Mona Rift, Western Puerto Rico: Eos (Transactions, American Geophysical Union), *Annual Fall Meeting*, F1181.
- Li, Z., E. J. Fielding, P. Cross, and J.-P. Muller (2006). Interferometric synthetic aperture radar atmospheric correction: GPS topography-dependent turbulence model, *J. Geophys. Res.* **111**, no. B2, doi: [10.1029/2005JB003711](https://doi.org/10.1029/2005JB003711).
- Liu, C., T. Lay, Z. Wang, and X. Xiong (2020). Rupture process of the 7 january 2020, Mw 6.4 puerto rico earthquake, *Geophys. Res. Lett.* **47**, no. 12, e2020GL087718 , doi: [10.1029/2020GL087718](https://doi.org/10.1029/2020GL087718).
- López, M. A., E. Vanacore, K. S. Hughes, G. Báez-Sánchez, and T. R. Hudgins (2020). Response and initial scientific findings from the southwestern Puerto Rico 2020 Seismic Sequence, doi: [10.32858/temblor.068](https://doi.org/10.32858/temblor.068).
- Mann, P., E. Calais, J.-C. Ruegg, C. DeMets, P. E. Jansma, and G. S. Mattioli (2002). Oblique collision in the northeastern Caribbean from GPS measurements and geological observations, *Tectonics*, **21**, no. 6, 7-1-7-26, doi: [10.1029/2001TC001304](https://doi.org/10.1029/2001TC001304).
- Mann, P., J.-C. Hippolyte, N. R. Grindlay, and L. J. Abrams (2005). Neotectonics of southern Puerto Rico and its offshore margin, in *Active Tectonics and Seismic Hazards of Puerto Rico, the Virgin Islands, and Offshore Areas*, Geological Society of America, doi: [10.1130/0-8137-2385-X.173](https://doi.org/10.1130/0-8137-2385-X.173).
- Mann, P., C. S. Prentice, J.-C. Hippolyte, N. R. Grindlay, L. J. Abrams, and D. Laó-Dávila (2005). Reconnaissance study of late quaternary faulting along Cerro Goden fault zone, western Puerto Rico, in *Active Tectonics and Seismic Hazards of Puerto Rico, the Virgin Islands, and Offshore Areas*, Geological Society of America, doi: [10.1130/0-8137-2385-X.115](https://doi.org/10.1130/0-8137-2385-X.115).
- Massonnet, D., M. Rossi, C. Carmona, F. Adragna, G. Peltzer, K. Feigl, and T. Rabaute (1993). The displacement field of the Landers earthquake mapped by radar interferometry, *Nature* **364**, no. 6433, 138–142, doi: [10.1038/364138a0](https://doi.org/10.1038/364138a0).
- Miller, S. A. (2020). Aftershocks are fluid-driven and decay rates controlled by permeability dynamics, *Nat. Commun.* **11**, no. 1, 5787, doi: [10.1038/s41467-020-19590-3](https://doi.org/10.1038/s41467-020-19590-3).
- Miranda, E., V. A. Acosta, L. Aponte, J. Archbold, M. Cortes, A. Du, S. Gunay, W. Hassan, P. Heresi, A. Lamela, et al. (2020). StEER—07 Jan. 2020 Puerto Rico Mw6.4 earthquake: Preliminary Virtual Reconnaissance Report (PVRR), doi: [10.17603/ds2-xfhz-fz88](https://doi.org/10.17603/ds2-xfhz-fz88).
- Mustać, M., B. Hejrani, H. Tkalčić, S. Kim, S. J. Lee, and C. S. Cho (2020). Large isotropic component in the source mechanism of the 2013 democratic people's Republic of Korea nuclear test revealed via a hierarchical Bayesian inversion, *Bull. Seismol. Soc. Am.* **110**, no. 1, 166–177, doi: [10.1785/0120190062](https://doi.org/10.1785/0120190062).
- Peacock, S. A. (1990). Fluid processes in Subduction zones, *Science* **248**, no. 4953, 329–337, doi: [10.1126/science.248.4953.329](https://doi.org/10.1126/science.248.4953.329).
- Piety, L. A., J. R. Redwine, S. A. Derouin, C. S. Prentice, K. I. Kelson, R. E. Klinger, and S. Mahan (2018). Holocene surface ruptures on the Salinas fault and southeastern great southern Puerto Rico fault zone, south coastal plain of Puerto Rico, *Bull. Seismol. Soc. Am.* **108**, no. 2, 619–638, doi: [10.1785/0120170182](https://doi.org/10.1785/0120170182).
- Prentice, C. S., and P. Mann (2005). Paleoseismic study of the South Lajas fault: First documentation of an onshore Holocene fault in Puerto Rico, in *Active Tectonics and Seismic Hazards of Puerto Rico, the Virgin Islands, and Offshore Areas*, P. Mann (Editor), Vol. 385, Geological Society of America, 215–222, doi: [10.1130/0-8137-2385-X.215](https://doi.org/10.1130/0-8137-2385-X.215).
- Roig-Silva, C., E. Asencio, and J. Joyce (2013). The northwest trending north Boquerón Bay-Punta Montalva Fault Zone; A through going active fault system in southwestern Puerto Rico, *Seismol. Res. Lett.* **84**, no. 3, 538–550, doi: [10.1785/0220120115](https://doi.org/10.1785/0220120115).
- Salichon, J., B. Delouis, P. Lundgren, D. Giardini, M. Costantini, and P. Rosen (2003). Joint inversion of broadband teleseismic and interferometric synthetic aperture radar (InSAR) data for the slip history of the Mw = 7.7, Nazca ridge (Peru) earthquake of 12 November 1996, *J. Geophys. Res.* **108**, no. B2, doi: [10.1029/2001JB000913](https://doi.org/10.1029/2001JB000913).
- Salichon, J., P. Lundgren, B. Delouis, and D. Giardini (2004). Slip history of the 16 October 1999 Mw 7.1 Hector Mine earthquake (California) from the inversion of InSAR, GPS, and teleseismic data, *Bull. Seismol. Soc. Am.* **94**, no. 6, 2015–2027, doi: [10.1785/0120030038](https://doi.org/10.1785/0120030038).
- Steinberg, A., H. Sudhaus, S. Heimann, and F. Krüger (2020). Sensitivity of InSAR and teleseismic observations to earthquake rupture segmentation, *Geophys. J. Int.* **223**, no. 2, 875–907, doi: [10.1093/gji/ggaa351](https://doi.org/10.1093/gji/ggaa351).
- Sudhaus, H., and S. Jónsson (2009). Improved source modelling through combined use of InSAR and GPS under consideration of correlated data errors: Application to the June 2000 Kleifarvatn earthquake, Iceland, *Geophys. J. Int.* **176**, no. 2, 389–404, doi: [10.1111/j.1365-246X.2008.03989.x](https://doi.org/10.1111/j.1365-246X.2008.03989.x).
- Symithe, S., E. Calais, J. B. de Chabalier, R. Robertson, and M. Higgins (2015). Current block motions and strain accumulation on active

- faults in the Caribbean, *J. Geophys. Res.* **120**, no. 5, 3748–3774, doi: [10.1002/2014JB011779](https://doi.org/10.1002/2014JB011779).
- ten Brink, U. S., and A. M. López-Venegas (2012). Plate interaction in the ne caribbean subduction zone from continuous gps observations, *Geophys. Res. Lett.* **39**, no. 10, doi: [10.1029/2012GL051485](https://doi.org/10.1029/2012GL051485).
- University of Puerto Rico (1986). Puerto rico seismic network and Puerto Rico strong motion program, *Int. Fed. Dig. Seismogr. Netw.* doi: [10.7914/SN/PR](https://doi.org/10.7914/SN/PR).
- United States Geological Survey (USGS) (2020). https://twitter.com/USGS_Quakes/status/1347203918678413313 (last accessed January 2021).
- Vasyura-Bathke, H., J. Dettmer, R. Dutta, P. M. Mai, and S. Jónsson (2021). Accounting for theory errors with empirical Bayesian noise models in nonlinear centroid moment tensor estimation, *Geophys. J. Int.* **225**, no. 2, 1412–1431, doi: [10.1093/gji/ggab034](https://doi.org/10.1093/gji/ggab034).
- Vasyura-Bathke, H., J. Dettmer, A. Steinberg, S. Heimann, M. P. Isken, O. Zielke, P. M. Mai, H. Sudhaus, and S. Jónsson (2019). BEAT—Bayesian earthquake analysis tool, GFZ Data Services, v.1.0, doi: [10.5880/fidgeo.2019.024](https://doi.org/10.5880/fidgeo.2019.024).
- Vasyura-Bathke, H., J. Dettmer, A. Steinberg, S. Heimann, M. P. Isken, O. Zielke, P. M. Mai, H. Sudhaus, and S. Jónsson (2020). The Bayesian earthquake analysis tool, *Seismol. Res. Lett.* **91**, no. 2A, 1003–1018, doi: [10.1785/0220190075](https://doi.org/10.1785/0220190075).
- Wang, G., H. Liu, G. S. Mattioli, M. M. Miller, K. Feaux, and J. Braun (2019). Carib18: A stable geodetic reference frame for geological hazard monitoring in the caribbean region, *Remote Sens.* **11**, no. 6, doi: [10.3390/rs11060680](https://doi.org/10.3390/rs11060680).
- Wang, R., S. Heimann, Y. Zhang, H. Wang, and T. Dahm (2017). Complete synthetic seismograms based on a spherical self-gravitating Earth model with an atmosphereocean-mantle-core structure, *Geophys. J. Int.* **210**, no. 3, 1739–1764, doi: [10.1093/gji/ggx259](https://doi.org/10.1093/gji/ggx259).
- Wang, R., M. F. Lorenzo, and F. Rot (2006). PSGRN/PSCMP—a new code for calculating co- and post-seismic deformation, geoid and gravity changes based on the viscoelastic- gravitational dislocation theory, *Comput. Geosci.* **32**, no. 4, 527–541, doi: [10.1016/j.cageo.2005.08.006](https://doi.org/10.1016/j.cageo.2005.08.006).
- Wegmüller, U. (1998). SAR Processing, Interferometry, Differential Interferometry and Geocoding Software, *EUSAR'98, Friedrichshafen, Germany*, VDE-Verlag, 25–27 May.
- Werner, C., U. Wegmüller, and T. Strozzi (2002). Processing strategies for phase unwrapping for INSAR applications, *Proceedings EUSAR Conference Cologne, Germany*.
- Yang, L., G. Wang, V. Huérano, C. G. von Hillebrandt-Andrade, J. A. Martínez-Cruzado, and H. Liu (2016). GPS geodetic infrastructure for natural hazards study in the Puerto Rico and Virgin Islands region, *Nat. Hazards* **83**, no. 1, 641–665, doi: [10.1007/s11069-016-2344-7](https://doi.org/10.1007/s11069-016-2344-7).

Manuscript received 14 September 2021

Published online 29 December 2021